LAWRENCE
LIVERMORE
NATIONAL
LABORATORY

The structure of turbulent flow at a river confluence with a momentum ratio close to one: insight provided by an eddy-resolving simulation

G. Constantinescu, S. Miyawaki, B. Rhoads, A. Sukhodolov, G. Kirkil

September 20, 2010

Disclaimer

This document was prepared as an account of work sponsored by an agency of the United States government. Neither the United States government nor Lawrence Livermore National Security, LLC, nor any of their employees makes any warranty, expressed or implied, or assumes any legal liability or responsibility for the accuracy, completeness, or usefulness of any information, apparatus, product, or process disclosed, or represents that its use would not infringe privately owned rights. Reference herein to any specific commercial product, process, or service by trade name, trademark, manufacturer, or otherwise does not necessarily constitute or imply its endorsement, recommendation, or favoring by the United States government or Lawrence Livermore National Security, LLC. The views and opinions of authors expressed herein do not necessarily state or reflect those of the United States government or Lawrence Livermore National Security, LLC, and shall not be used for advertising or product endorsement purposes.

THE STRUCTURE OF TURBULENT FLOW AT A RIVER CONFLUENCE WITH A MOMENTUM RATIO CLOSE TO ONE: INSIGHT PROVIDED BY AN EDDY-RESOLVING NUMERICAL SIMULATION

George Constantinescu, Shinjiro Miyawaki, Bruce Rhoads, Alexander Sukhodolov and Gokhan Kirkil

Abstract

River confluences are complex hydrodynamic environments where convergence of incoming flows produces complicated patterns of fluid motion, including the development of large-scale turbulence structures. Accurately simulating confluence hydrodynamics represents a considerable challenge for numerical modeling of river flows. This study uses an eddy-resolving numerical model to simulate the mean flow and large-scale turbulence structure at an asymmetrical river confluence with a concordant bed when the momentum ratio between the two incoming streams is close to one. Results of the simulation are compared with field data on mean flow and turbulence structure. The simulation shows that the mixing interface is populated by quasi two-dimensional (2D) eddies. Successive eddies have opposing senses of rotation. The mixing layer structure resembles that of a wake behind a bluff body (wake mode). Strong streamwise-oriented vortical (SOV) cells form on both sides of the mixing layer – a finding consistent with patterns inferred from the field data. The predicted mean-flow fields show that flow curvature has an important influence on streamwise variation of circulation within the cores of the two primary SOV cells. These SOV cells, along with vortices generated by flow over a submerged block of sediment at one of the banks, strongly influence distributions of the streamwise velocity and turbulent kinetic energy downstream of the junction. Comparison of the eddy resolving simulation results with predictions from a steady RANS model shows that the latter fails to predict important features of the measured distributions of streamwise velocity and turbulent kinetic energy because the RANS model underpredicts the strength of the SOV cells. Analysis of instantaneous and mean bed shear stress distributions indicates that the SOV cells enhance bed shear stresses to a greater degree than the quasi-2D eddies in the mixing interface.

29

30   **1. Introduction**

31   Stream confluences are elements of river networks that play a major role in the dynamics of

32   fluvial systems. Substantial changes in flow hydrodynamics and bed morphology generally occur

33   within and immediately downstream of junctions, a region referred to as the confluence

34   hydrodynamic zone (CHZ) [*Kenworthy and Rhoads*, 1995], and mixing of tributary flows may extend

35   many kilometers downstream of confluences [*Bouchez, et al.*, 2010, *MacKay*, 1970]. A considerable

36   amount of research has been conducted during the last few decades to elucidate the mechanisms

37   controlling flow structure, sediment movement, channel change, bed material distributions, and flow

38   mixing at stream confluences [*Best*, 1987; *Best*, 1988; *Best and Reid*, 1984; *Best and Rhoads*, 2008 ;

39   *Biron, et al.*, 1993a; *Biron, et al.*, 1993b; *Biron, et al.*, 2004; *Biron, et al.*, 2002; *Bradbrook, et al.*,

40   2000a; *Bradbrook, et al.*, 2001; *Rhoads and Kenworthy*, 1998; 1999; *Rhoads and Sukhodolov*, 2001;

41   2004; 2008; *Sukhodolov and Rhoads*, 2001; *Weerakoon and Tamai,* 1989]. This body of work has

42   shown that confluence hydro- and morphodynamics are complex. In general, flow structure and

43   patterns of erosion and deposition at junctions are mainly controlled by the momentum ratio between

44   the two tributaries, by the magnitude and ratio of the angles between the tributaries and the

45   downstream channel, and by the degree of concordance of the channel beds at the entrance to the

46   confluence. However, details of turbulence and of the mean flow within confluences as well as

47   contributions of different aspects of the flow to bed shear stresses have yet to be fully resolved.

48   The purpose of this paper is to use an eddy-resolving numerical model, specifically detached

49   eddy simulation (DES), to examine details of turbulent flow structure with an asymmetrical (γ-

50   shaped) stream confluence when the momentum ratio between the incoming flows is close to one.

51   The predictive capabilities of the model are evaluated by comparing the simulated flow characteristics

52   against velocity data collected in the field. The need for an eddy-resolving model to accurately capture

53   details of mean flow and turbulence is assessed by comparing predictions of the DES model against

54   those for a model without eddy-resolving capabilities. The contributions of different aspects of the

55   predicted flow field to the pattern of bed shear stresses are also determined.

2. Flow Structure at Confluences

Flow structure within the CHZ at confluences with an asymmetrical planform is characterized by a variety of hydrodynamic zones, including flow stagnation near the upstream junction corner, the development of a mixing interface between the two confluent flows, possible flow separation below the downstream junction corner, flow acceleration in the downstream channel, and flow recovery at the downstream end of the CHZ [*Best*, 1987]. A focus of particular interest has been the structure of turbulence within the mixing interface [*Biron, et al.*, 1993a; *Bradbrook, et al.*, 2000b; *Rhoads and Sukhodolov*, 2004; 2008]. In addition, the development of helical motion in the form of twin streamwise vortical cells (SOVs) has been documented at some [*Ashmore, et al.*, 1992; *Rhoads*, 1996; *Rhoads and Kenworthy*, 1998; *Rhoads and Sukhodolov*, 2001], but not all [*De Serres, et al.*, 1999; *Parsons, et al.*, 2007] confluences. As a result, the occurrence of SOVs at confluences has been controversial [*Lane, et al.*, 2000; *Rhoads and Kenworthy*, 1999].

2.1. Mixing Interface

A key hydrodynamic characteristic of confluences is the formation of a mixing interface between the converging flows and the development of large-scale coherent turbulence structures within this interface [*Sukhodolov and Rhoads*, 2001]. The position of the mixing interface is mainly dependent on the momentum ratio between the two tributaries and the angle between the axes of the two tributaries and that of the downstream channel [*Best*, 1987]. Abrupt changes in the bathymetry (e.g., bed discordances between the tributaries and the downstream channel) can also have a significant effect on the position and rate of lateral expansion of the mixing interface [*Boyer et al., 2006*]. The large width to depth ratio of many natural channels induces significant changes in the development of shallow mixing layers over large distances compared to the case of a free mixing layer. The large-scale turbulence within most shallow mixing layers, including mixing interfaces at confluences, has been described as predominantly quasi two-dimensional (2D) [*Babarutsi and Chu*, 1998]. Energy is transported from small scales toward the large-scale quasi-2D eddies through an inverse cascade. Shallow mixing-layer eddies have axes that are close to vertical and their characteristics vary little over the vertical direction until close to the bed, where 3D effects become important.

84   Theoretical considerations from fluid mechanics on how mixing layers develop in shallow

85   shear flows provides the basis for classifying confluence mixing interfaces into two types, depending

86   on their hydrodynamic characteristics. When the momentum ratio between the two tributaries is

87   much larger than unity, the growth of the eddies inside the mixing interface should be driven by the

88   Kelvin-Helmholtz instability, similar to a shallow mixing layer developing between two parallel

89   streams of different bulk velocities. Under such conditions, mixing-interface eddies will be quasi two-

90   dimensional and co-rotating. The main mechanism for the increase of the mixing-interface width is

91   vortex pairing, or the amalgamation of successive eddies [*Winant and Browand*, 1974]. Such a mixing

92   interface is in the **Kelvin-Helmholtz (KH) mode**.

93   When the momentum ratio between the two streams is close to unity and the junction angle is

94   large, the KH instability will be weak because mean shear between the flows will be limited and the

95   development of a stagnation zone at the upstream junction corner will influence vortex development.

96   Under such conditions, the mixing interface will be populated by successive vortices rotating in

97   opposite directions (alternating vorticity). These vortices form as a result of the interaction between

98   the shear layers bounding and detaching from the stagnation zone. In this case, the mechanism for the

99   formation of the quasi 2D-vortices is similar to the process of vortex shedding responsible for the

100   development of the von Karman vortex street behind a bluff body. The exact geometry of the

101   separation zone near the upstream junction corner controls the way the two separated shear layers

102   interact and, ultimately, the strength (e.g., measured by the circulation) of the vortices shed into the

103   mixing interface. Under these conditions, the mixing layer is in the **wake mode** and the rate of growth

104   of the mixing-interface width is small compared to that of a mixing interface in the KH mode.

105   Theses modes of mixing-interface dynamics are not necessarily mutually exclusive. The

106   formation of a separation zone near the upstream junction corner at a high-angle confluence with a

107   high momentum ratio may lead to co-production of vortices from KH-mode and wake-mode

108   processes. The details of mixing interface dynamics are difficult to ascertain from field or laboratory

109   studies based on relatively sparse measurements at particular points in the interface at particular times.

110   Numerical simulations that allow eddies within the mixing interface to be resolved in considerable

111   detail provide a scientific tool for exploring the structure of turbulence within the mixing interface,

112 including the development and evolution of coherent eddies and the interaction of these eddies with

113 the mean flow, including coherent three-dimensional fluid motion within this flow. Of particular

114 interest is the use of hybrid RANS (Reynolds-Averaged Navier Stokes)-LES (Large Eddy Simulation)

115 methods like Detached Eddy Simulation (DES0 [*Spalart, 2009*]) that allow simulations of field

116 conditions while resolving the dynamically important coherent structures in the flow.

117

118 *2.2 SOV Cells*

119   Besides the turbulent eddies in the mixing interface, another type of coherent structure greatly

120 affects momentum and mass exchange processes where the angle between the two tributaries is

121 relatively large, as is often the case for natural river confluences. Coherent streamwise-oriented

122 vortical (SOV) cells of helical motion may form adjacent to the mixing interface *[Rhoads and*

123 *Kenworthy, 1995, 1998, Rhoads, 1996, Paola, 1997*]. Loss of kinetic energy in the converging flows,

124 especially in the region near the junction apex where low-velocity fluid along the channel banks

125 meets, produces an increase of pressure and superelevation of the free surface [*Bradbrook, et al.*,

126 2000a]. The region of superelevation varies depending on the total momentum flux and flux ratio of

127 the two flows, but roughly coincides with the upstream part of the mixing interface. The raised free

128 surface elevation induces vertical motion of fluid toward the bed. As flow approaches the bed, it

129 moves laterally away from the mixing interface toward each bank and then upward toward the

130 surface. The result is a pair of counter-rotating vortices with streamwise axes flanking the mixing

131 interface. The relative strengths (e.g., as measured by their circulation and the streamwise distance

132 over which they maintain their coherence) depend mainly on the angles between the two tributaries

133 and the downstream channel and the momentum ratio between the two tributaries. At asymmetrical

134 confluences, the strength of the cell on the tributary side of the confluence, where flow must turn

135 abruptly to enter the downstream channel, should generally exceed the strength of the counter-

136 rotating cell on the main-stream side of the confluence [*Rhoads*, 1996]. Increases in junction angle

137 and momentum ratio will increase cell strength on the tributary side of the confluence.

138   Though the broad patterns of the secondary flow can be inferred from 3D measurements

139 obtained in the field (e.g., Rhoads and Sukhodolov, 2001), the density of spatial information,

140 especially in the spanwise direction, does not generally allow a detailed characterization of the

141 secondary flow over the whole section and accurate identification of the position and distribution of

142 the vorticity associated with helical cells in that section. The streamwise resolution is low compared

143 to the transverse resolution because the density of measurements in the streamwise direction is much

144 less than in the transverse direction when data are collected at cross sections. Thus, determining with

145 high accuracy the position of SOVs in the mean flow with respect to the bed and to the mixing

146 interface as well as the streamwise variation of SOV circulation based on field measurements is a

147 challenging task. A highly-resolved numerical simulation allows three-dimensional large-scale

148 coherent structures in the mean flow to be resolved in much greater detail than can be achieved with

149 field measurements. This capability is important not only for the characterization of flow within the

150 SOV cells, but also for characterization of vortical structures that may be generated by local effects,

151 such as irregular bathymetry and bank alignments, that can affect the streamwise evolution of the

152 mean flow at natural confluences. Moreover, detailed numerical simulations can be used to examine

153 variation of the mean flow and turbulence over the entire flow depth, including the near-bed layer,

154 where large scale coherent structures (e.g., mixing layer eddies, SOV cells) interact with the bed.

155 Such analysis is essential for understanding the mechanisms responsible for patterns of bed shear

156 stresses, which in turn can be linked to sediment entrainment and maintenance or change in bed

157 morphology. Eddy-resolving simulations allow concomitant visualization of coherent structures and

158 bed shear stress distributions in the mean and instantaneous flow fields, allowing effects of various

159 structures (SOVs, quasi-2D unsteady eddies) on patterns of bed shear stress to be explored.

160

161 **3. Study Site**

162 The numerical simulation focuses on flow structure at the confluence of the Kaskaskia River

163 and the Copper Slough (KRCS) - an asymmetrical confluence with concordant bed that has been the

164 focus on a considerable body of field work on confluence dynamics [*Rhoads*, 1996; *Rhoads and*

165 *Kenworthy*, 1995; 1998; *Rhoads and Sukhodolov*, 2001; 2004; 2008; *Sukhodolov and Rhoads*, 2001].

166 The confluence has an asymmetrical planfrom with the upstream channel for the Kaskaskia River

167 aligned with the downstream channel and the Copper Slough joining the Kaskaskia River at an angle

168   of about 60^0. The flow simulated in this study corresponds to conditions at the site on May 27, 1998

169   when characteristics of mean flow and turbulence were documented with field measurements [*Rhoads*

170   *and Kenworthy*, 1998; *Rhoads and Sukhodolov*, 2001; *Sukhodolov and Rhoads*, 2001]. On this date,

171   the momentum ratio between the two incoming streams was close to one (1.03). The bed was not

172   mobile during the conditions simulated here and thus sediment transport and changes in bed

173   morphology are not considered. However, patterns of bed shear stress are predicted to explore how

174   patterns of flow and turbulence are associated with the spatial distribution of bed morphology at the

175   confluence.

176

4. Numerical model

178   The hybrid RANS-LES model used to perform the eddy-resolving simulation is called Detached Eddy

179   Simulation (DES). The hybrid model uses the same base turbulence model in the RANS and LES

180   regions. No special treatment is required to match the solutions at the boundary between the LES and

181   RANS regions. The governing equations are integrated through the viscous sub-layer and no wall

182   functions are used. The Spalart-Allmaras (SA) RANS model serves as the base model in DES

183   [*Spalart, 2000*]. The one-equation SA model solves a transport equation for the modified eddy

184   viscosity, $\tilde{v}$. The SA version of DES is obtained by replacing the turbulence length scale d (distance

185   to the nearest wall) in the destruction (dissipation like) term of the transport equation for $\tilde{v}$ with a new

186   length scale d_{DES}=min(d,$C_{DES}\Delta$), where the model parameter C_{DES} is equal to 0.65 and Δ is a measure

187   of the local grid size. When the production an destruction terms in the transport equation for $\tilde{v}$ are

188   balanced, the length scale in the LES regions d_{DES}=$C_{DES}\Delta$ becomes proportional to the local grid size

189   and yields an eddy viscosity proportional to the mean rate of strain and Δ^2 as in LES with a

190   Smagorinsky model. This method allows a cascade of energy down to grid size. The boundary

191   condition implementation for rough walls is described in Spalart (2000).

192   A general description of the code, governing equations and DES model used to perform the

193   eddy resolving simulation are given in Constantinescu and Squires (2004) and Chang et al. (2007).

194   The incompressible Navier-Stokes equations are integrated using a fully-implicit fractional-step

195 method. The governing equations are formulated in generalized curvilinear coordinates on a non-

196 staggered grid. The convective terms in the momentum equations are discretized using the fifth-order

197 accurate upwind biased scheme. All the other terms in the momentum and pressure-Poisson equations

198 are approximated using second-order central differences. The discrete momentum (predictor step)

199 and turbulence model equations are integrated in pseudo-time using the alternate direction implicit

200 (ADI) approximate factorization scheme. Time integration in the DES code is done using a double

201 time-stepping algorithm. The time discretization is second-order accurate. The simulations were

202 performed using a parallel (MPI) version of the code.

203 Results of grid sensitivity and validation studies for simulations of channel flow over a

204 bottom cavity and flow past hydraulic structures (e.g., groynes, bridge piers in channels with flat and

205 scoured bed) conducted using the same code are discussed by Chang et al. (2007), Kirkil et al. (2009),

206 Kirkil and Constantinescu (2009) and Koken and Constantinescu (2009). Also, Kirkil and

207 Constantinescu (2008) applied the code to study the streamwise development and turbulence structure

208 of a mixing layer developing downstream of a splitter plate separating two turbulent streams of

209 unequal velocities in a flat bed channel at a relatively low channel Reynolds number (Re~18,000).

210 This test case is a limiting case for a river confluence with concordant bed in which the angles

211 between the two tributaries and the downstream channels are close to zero and the mixing layer is in

212 KH mode. The DES model successfully captured the streamwise variation in the centerline

213 displacement and width of the shallow mixing layer, as well as the mean flow streamwise velocity

214 variation across the mixing layer at the stations where experimental measurements were available.

215 Consistent with the experimental data, analysis of the velocity spectra confirmed the quasi-2D

216 character of the turbulence within the region where the cores of the KH billows become much larger

217 than the channel depth.

218

219 **5. Simulations set up**

220 The flow at the confluence of Kakaskia River (west [W] side of the confluence) and Copper

221 Slough (east [E] side of the confluence) on May 27, 1998 is simulated using DES and RANS models.

222 To allow a direct comparison of the capability of DES and RANS models to predict the mean flow

223 and turbulence quantities within the confluence region, the two simulations were run on the same

224 mesh using the same code and base turbulence model (SA). The mesh and upstream flow boundary

225 conditions were established from field data on bathymetry and incoming flow collected during the

226 field experiment [*Rhoads and Sukhodolov*, 2001; *Sukhodolov and Rhoads*, 2001].

227   The cross sections of both tributaries upstream of the confluence are trapezoidal. The channel

228 beds within the confluence are concordant, but a submerged block of failed bank material is present

229 along the west bank of the confluence close to where the Kaskaskia River enters the junction (see Fig.

230 1). On the east side, bank curvature at the entrance into the main downstream channel is high. The

231 radius of curvature of the flow around this curved bank divided by the mean width of the downstream

232 channel is close to 3.5. Given the curvature of the downstream channel, the inner and the outer banks

233 correspond to the east (E) and the west (W) banks, respectively.

234   The mean flow velocities in the two tributaries are U_W=0.42 m/s and U_E=0.46 m/s. The

235 average flow depths in the two tributaries are D_W=0.48 m and D_E=0.3 m. The velocity and length

236 scale used to non-dimensionalize the flow variables are U=0.45 m/s and D=0.36 m, respectively. The

237 value of D is close to the average flow depth in the downstream channel, except for depths inside the

238 scour hole. The maximum flow depth inside the scour hole is close to 3D and is located at a distance

239 of about one and a half times the average downstream-channel width (W) from the upstream junction

240 corner (Fig. 1). The Reynolds number and the Froude number defined with D and U are 166,000 and

241 0.24, respectively. The incoming discharges are Q_W=1.41 m^3/s and Q_E=1.34 m^3/s, such that the

242 momentum ratio M_r=$(\rho E_E Q_E U_E)/(\rho_W Q_W U_W)$ is close to unity (M_r = 1.03). Thus, transverse shear

243 should have a negligible effect on the development of the mixing interface between the two streams.

244   The wall-normal grid spacing of the first row of cells off the bed and channel sidewalls was

245 close to two wall units. Using information from the field study, the mean value of the bed roughness

246 height was estimated to be 0.01 m. The channel bed and sidewalls were treated as rough no-slip

247 boundaries. At the two inflow sections, inflow conditions corresponding to fully-developed turbulent

248 channel flow were applied in the DES and RANS simulation. In the DES, the velocity fields

249 containing resolved turbulence obtained from preliminary periodic channel simulations were stored in

250 a file and then fed in a time-accurate manner through the two inflow sections. In the RANS

251 simulation, the distributions of the mean velocity and eddy viscosity in the two inflow sections were

252 obtained from preliminary steady RANS runs of fully developed turbulent channel flow. At the

253 outflow, a convective boundary condition was used. The free surface was treated as a rigid lid, which

254 is justified as the Froude number in the field experiment was much smaller than 0.5. The

255 computational domain was meshed with 4.5 million cells. The physical time step in DES was close to

256 0.1 D/U.

257

258 **6. Results**

259 *6.1 Vortical structure of the flow: DES and comparison with RANS simulation*

260 The DES-predicted vortical structure of the instantaneous flow close the free surface (see Fig.

261 2), based on the distribution of the vertical component of the vorticity vector, $\omega_z D/U$, clearly shows

262 the development of the mixing interface between the two flows. The geometry of the banks close to

263 the upstream junction corner is such that the boundary layer on the CS side separates before the

264 confluence apex, while the one on the KR side remains attached until the confluence apex. This

265 relation between the streams holds not only close to the free surface, but also at deeper levels of the

266 flow (e.g., see Fig. 3). A small stagnation zone of separated, recirculating flow, characterized by

267 vorticity of opposite signs, forms between the confluence apex and the two separated shear layers.

268 The distributions of ω_z show that the size of the stagnation zone in the mean flow remains constant

269 over depth, at least until close to the bed (Fig. 3). Temporal distributions of ω_z indicate that the two

270 separated shear layers near the confluence apex interact in such a way that elongated patches of

271 vorticity detach from their downstream ends. This vortex shedding explains why the mixing interface

272 between the two streams is populated by highly-energetic vortical eddies containing positive and

273 negative vorticity. Moreover, as the eddies are convected downstream, the alternating patches of

274 positive and negative vorticity become more circular (e.g., downstream of section A1 in Fig. 2). At

275 this point, the structure of the mixing interface becomes similar to that in a wake forming behind a

276 bluff body, confirming that the interface is in the wake mode.

277   In the upstream part of the confluence (between A2 and B) , the mean streamwise velocity, u_s,

278   on the west side of the mixing interface is larger than that on the east side of the interface (e.g., see

279   Figs. 7 and 8 showing distribution of u_s in sections A1 and A). The maximum difference between u_s

280   on the two sides of the mixing interface is of the order of 5-10% close to the free surface. Thus,

281   differential shear is expected to play a small role in the development of the mixing interface eddies at

282   the free surface. At deeper levels, the streamwise velocity is generally larger inside the mixing

283   interface compared to the adjacent regions. Thus, despite the fact that $M_r{\sim}1$, the KH mode is still

284   present in some regions of the mixing interface, though it is much weaker than the wake mode.

285   The instantaneous vorticity distribution (Fig. 2) can be used to approximately estimate the

286   streamwise variation of the width of the mixing interface and the position of its centerline. Consistent

287   with the field measurements, the mixing-interface centerline is situated within the central part of the

288   downstream channel, at least until section C. For a mixing interface that is predominantly in the KH

289   mode, one can define its width based on the maximum slope in the cross-stream profile of streamwise

290   velocity [Chu and Babarytsi, 1988]. Such a definition does not apply for the case in which the wake

291   mode is dominant. More generally, one can define the mixing interface thickness as the width of the

292   region in which mixing-interface vortices are present. As expected, the mixing interface thickness at

293   KRCS increases with the distance from the upstream junction corner. For a shallow plane mixing

294   layer downstream of a splitter plate between parallel flows, the size of eddies and the thickness of the

295   mixing layer continue to increase until bed friction effects becomes so important that the coherence of

296   these eddies is lost [*Chu and Babarutsi*, 1988]. The evolution of the mixing interface at the KRCS

297   confluence is more complex than that for a simple shallow mixing layer. The interactions of the

298   mixing-interface eddies with the strongly energetic eddies generated by the convection of the flow

299   over the submerged block of failed bank material near section A3 (see Fig. 1) and with the shear layer

300   generated by sharp curvature of the inner bank between sections A2 and B limit the growth of the

301   thickness of the mixing interface downstream of section B. Meanwhile, in contrast to experimental

302   findings on mixing-layer development in depth-limited flows [*Chu and Babarutsi*, 1988], bed friction

303   effects are not strong enough to limit the rate of growth of the mixing interface thickness within the

304   CHZ (Fig. 2).

305   The dominant frequency of passage of the mixing-interface eddies is close to 0.15 D/U.

306   Analysis of the vorticity fields at different levels shows the axes of the eddies remain close to vertical

307   even at large distances from the upstream junction corner – a finding consistent with the field data

308   [*Sukhodolov and Rhoads*, 2001]. Velocity spectra inside the mixing interface include a low-frequency

309   -3 subrange, a result also consistent with field data [*Rhoads and Sukhodolov*, 2004]. The presence of a

310   -3 subrange is associated with inverse energy cascade in which energy is transported in average from

311   smaller scales toward the larger quasi-2D mixing interface eddies. This outcome is consistent with the

312   fact that the large-scale mixing layer eddies are quasi 2D in the regions where their interactions with

313   other large-scale coherent structures is not significant.

314   Though the flow does not separate from the east bank, the strong curvature of this bank

315   between sections A3 and B induces the formation of a thin shear layer of high (positive) vorticity

316   separating the core of high streamwise velocity from the CS tributary and the region of low

317   streamwise velocity situated close to the bank. As shown in Figs. 2 and 3, near the free surface, the

318   shear layer originating at the east bank extends well into the main flow and interacts with the mixing-

319   interface eddies around section C. This interaction is also confirmed by the distribution of the vertical

320   vorticity in the mean flow (Fig. 3). The shear layer is not uniform over the channel depth. As shown

321   in Fig.3, as one moves toward the bed, the shear layer gets closer to the inner bank. For example, at

322   0.5D below the free surface, the shear layer, though clearly distinct from the attached boundary layer

323   on the inner bank, follows closely the bank line. At even deeper levels, the shear layer is not present.

324   The formation of a strong shear layer at the inner bank with the aforementioned characteristics is a

325   common feature of flow in bends of medium and high curvature (Zeng et al., 2008). In some cases

326   flow can even separate at the inner bank of a strongly curved bend (e.g., Bagnold, 1960; Ferguson et

327   al., 2003, Zeng et al., 2008).

328   A region of shallow flow along the west bank close to section A3, which corresponds to a

329   submerged block of failed bank material, induces the formation of two shear layers. The first one is a

330   predominantly vertical, originates at the lateral extremity of the block, and extends from the channel

331   bottom up to the crest of the obstruction. The second one is predominantly horizontal and originates at

332   the crest of the block. The upstream part of the vertical shear layer is nicely visualized in the mean

333 flow vorticity distribution at 0.5D below the free surface (Fig. 3). Eddies shed in the horizontal shear

334 layer can reach both the free surface and the channel bed at sufficient large distances from the crest of

335 the submerged block. As a result, the region downstream of section A2 between the high velocity core

336 of the Kaskasia River and the west bank is populated by strongly energetic vortical eddies (Fig. 2).

337 These eddies start interacting with the mixing interface eddies past section A. Finally, a tip vortex

338 (TV1 in Fig. 4) originates at the corner between the top and lateral faces of the submerged block. The

339 mechanisms responsible for the formation of the horizontal and vertical shear layers and the tip vortex

340 are similar to the ones responsible for the formation of such structures in flow past submerged dike-

341 like structures. McCoy et al. (2007) provide a detailed discussion of these mechanisms.

342 Downstream of section C eddies shed within the shear layers originating close to the two

343 banks are as energetic as the vertically oriented eddies inside the mixing interface (Fig. 2). Moreover,

344 these locally generated eddies strongly disturb the mixing interface as they jitter and sometimes merge

345 with the mixing-interface eddies. The local flow structure is highly three-dimensional. Thus, the

346 structure of the mixing interface developing downstream of section A is more complex than that

347 expected to occur in a wide stream of relatively low curvature in which interactions with large-scale

348 turbulence originating at the banks is not significant.

349 The Q criterion [*Dubief and Delcayre,* 2000] provides the basis for visualizing the main

350 vortical structures in the mean flow for the DES simulation (Fig. 4). The dominant vortical structures

351 are two primary counter-rotating SOV cells forming on the inner (SVI1) and outer (SVO1) sides of

352 the mixing interface. Secondary SOV cells (SVI2 and SVO2) containing vorticity of the same sign to

353 that in the primary cells are also present on both sides of the mixing interface. The secondary cells

354 decay much faster than the primary SOVs, especially the secondary SOV on the outer (west) side of

355 the downstream channel. The dominant vorticity component within the SOV cells is oriented parallel

356 to the local streamwise direction. The streamwise-oriented vorticity, $\omega_s D/U$, and the Q isosurface are

357 used to visualize the cores of the SOV cells, the vorticity distribution within their cores, and their

358 position relative to the mixing interface (Fig. 5). The cores of the SOV cells are fairly circular. The

359 high concentration of vorticity within the sections where the SOVs are strongly coherent and the

360 closeness of the cores of the SOVs to the channel bottom induce the ejection of patches of vorticity

361   from the bottom-attached boundary layer and the formation of weaker bottom-attached streamwise-

362   oriented vortices. The primary SOVs extend over most of the height of the water column and remain

363   close to the mixing interface at all the sections where their coherence is high. As expected, their

364   circulation is such that they induce a strong downward movement of the fluid within the mixing

365   interface [*Rhoads,* 1996, *Paola*, 1997]. Besides the SOV cells and the tip vortex TV1, a weak

366   streamwise-oriented vortex forms, starting at section A1, within the region bordered by the shear layer

367   induced by curvature of the inner (east) bank of the downstream channel, the free surface and the east

368   bank.

369   The mean-flow vorticity patterns indicate that the mixing interface does not contain many

370   large-scale coherent structures. This finding is not unexpected because in a certain region within the

371   mixing interface alternating quasi-2D eddies with vorticity of opposite sign are convected at relatively

372   regular time intervals. The cancellation of the vorticity by successively shed vortices and the low

373   vorticity values at time instants when no vortices are convected in that region explain the low values

374   of vorticity in the mean flow. The coherence of the quasi-2D eddies within the mixing interface

375   remains relatively low compared to that of the SOV vortices even in the instantaneous flow fields.

376   Because the wake mode is dominant, vortex pairing does not occur and no mechanism exists to

377   increase the coherence of mixing-interface eddies as they are convected downstream.

378   The ratio between the circulation of the two primary SOV cells, $\Gamma_{SVI1}/\Gamma_{SVO1}$, varies

379   significantly with non-dimensional streamwise distance measured from the confluence apex, s/W

380   (W=14D is the average width of the downstream channel) (Fig. 6). At section A3, which is situated

381   close to the upstream junction corner, Γ_{SVI1} is about three times larger than -Γ_{SVO1}. This difference is

382   not surprising given the asymmetrical planform geometry of the confluence. Flow from the Copper

383   Slough must turn to become aligned with downstream channel, whereas flow entering the confluence

384   from the Kaskaskia River (KR) is already aligned with the downstream channel. Thus, the SOV cell

385   on the KR side is expected to be weaker than the cell on the CS side. Within the confluence, the

386   mixing interface is pushed toward the west bank, deflecting flow from the KR outward and causing

387   curvature of flow on the west side of confluence that opposes curvature of flow on the east side. The

388   effect is similar to two meander bends placed "back to back" [*Ashmore and Parker*, 1983]. Curvature

389   of flow on the west side increases the magnitude of Γ_{SVO1}. Consequently, the ratio -$\Gamma_{SVI1}/\Gamma_{SVO1}$ decays

390   over distance between the upstream junction corner and section A1, where $\Gamma_{SVI1} \cong$ -$\Gamma_{SVO1} \cong 1.0D/U$.

391   Downstream of section A1, curvature of flow from the Copper Slough around the

392   downstream junction corner along with mild curvature of the downstream channel amplifies the

393   strength of the SOV cells rotating counter-clockwise (SVI1 and SVI2) and decreases the strength of

394   the SOV cells rotating clockwise (SVO1). In addition, interaction of SVI1 and SVO1 with eddies

395   originating from near-bank shear layers results in jittering of the SOV cores and decreases in the

396   coherence of the SOV cells. The level of interaction between the eddies shed within the shear layers

397   forming downstream of the submerged bar of failed bank material and SVO1 is much larger than the

398   level of interaction between the shear layer originating at the inner bank, close to section A1, and

399   SVI1. This effect contributes to the diminution of circulation of SVO1 at a faster rate than that of

400   SVI1. These interactions start around section B for eddies induced by the failed bank material and

401   around section C for the shear layer originating at the inner bank (see Fig. 2). The net result of

402   curvature-induced and local effects is an increase of -$\Gamma_{SVI1}/\Gamma_{SVO1}$ from around 1.0 at section A1 to

403   close to 1.5 at sections B and C, and a rapid decay in the circulation of SVO2, which loses most of its

404   coherence by the time it reaches section C. The change from counter-rotating cells upstream to a

405   dominant counterclockwise rotation downstream generally conforms to the conceptual model of

406   helical motion at this confluence proposed by Rhoads (1996) for $M_r \leq 1$. It is also consistent with

407   observed patterns of sediment sorting at this confluence for $M_r \approx 1$ [*Rhoads et al.*, 2009].

408   Figure 4 provides a comparison between the coherent structures predicted by the DES (mean

409   flow) and by a steady RANS simulation. The same value was used for the Q isosurface to visualize

410   the coherent structures in the two simulations. Regarding the SOV cells, the most striking difference

411   is the large underprediction of the coherence of SVO1 and SVI1 in the RANS simulation compared to

412   DES. No SOV cell corresponding to SVI2 is observed in the RANS simulation.

413

414   *6.2. Streamwise velocity and turbulent kinetic energy: DES versus RANS*

415   To evaluate the predictive capabilities of the DES and RANS models, the distributions of the

416 mean streamwise velocity u_s (m/s) at sections A1, A and C and of the TKE at sections A3, A1, A and

417 C are compared to the distributions of these variables from the field measurements (Figures 7-11).

418 The positions of the main SOV cells are also shown in the DES plots. The aspect ratio of the plots is

419 distorted in the vertical direction to allow direct comparison with the field data and to better visualize

420 the vertical variation of these variables in each cross section.

421   In agreement with the field measurements, DES predicts larger values of u_s over the west side

422 of section A1 (Fig. 7). Also, the region of relatively high u_s values extends close to the bed in the

423 central part of the section, corresponding to the mixing interface. The primary counter-rotating SOV

424 cells induce strong downwelling of the flow within the mixing interface. These cells advect near-

425 surface fluid with high streamwise velocities toward the bed and then outward toward the two banks.

426 Despite the fact that the absolute values of the circulations of SVO1 and SVI1 at section A1 are nearly

427 equal, downwelling flow within the mixing interface is convected predominantly toward the east bank

428 as it reaches the near-bed region. This net inward flow can be attributed to the strong circulation of

429 SVI2 in section A1; the total circulation induced by the primary and secondary SOV cells on the east

430 side of the section is larger than the circulation induced by the SOV cells on the west side of the

431 section. Although the RANS correctly predicts larger values of u_s on the west side of the section than

432 on the east side, the overall shape of the core of high u_s values on the west side of section A1 and the

433 peak values of u_s within the core (u_s~0.6 m/s) are more accurately captured by DES.

434   The distributions of u_s predicted by DES and as determined from the field measurements

435 contain two distinct regions of large streamwise velocities within the upper part of section A (Fig. 8).

436 The size of the region of high u_s values (u_s>0.5 m/s) on the west side of section A and the peak value

437 of u_s within this region are larger (by about 20% for the peak value) then the size and peak values of

438 the region of high u_s on the east side of section A. Both of these features of the distributions of u_s

439 predicted by DES are in good agreement with the field measurements. As $\Gamma_{SVI1} = -1.15\Gamma_{SVO1}$ at section

440 A, the core of high u_s values is displaced toward the east bank in the deeper part of the section. The

441 cores of the SOVs and the region between these cores have values of u_s that are slightly smaller than

442 those in the surrounding flow. In agreement with the field data, DES predicts that the mixing interface

443   at section A is a region of relatively high u_s values. In contrast, the RANS model does not predict two

444   regions of relatively high u_s values close to the free surface as is evident in the field data. The

445   distributions of u_s on the two sides of the section are close to identical and are characterized by

446   gradual variation of u_s away from the bed and the channel bottom. The primary SOV cells predicted

447   by the RANS simulation are much less coherent than those in DES. The circulation of cells in the

448   RANS simulation is not strong enough to convect substantial amounts of near-surface streamwise

449   momentum toward the bed.

450   At section C (Fig. 9), both DES and the field measurements show only a single region of high

451   u_s values within the central part of the section. Consistent with stronger circulation of SVI1 compared

452   to SVO1 (Γ_{SVII}=-1.5Γ_{SVO1}), the high-velocity region extends over virtually the entire east side of the

453   section. Most of the fluid convected downwards toward the bed in the central part of the section

454   moves beneath the core of SVI1 and then upwards toward the free surface on the east side of this

455   helical cell. The efficiency of SVI1 in convecting more of the high streamwise velocity fluid toward

456   the east bank is enhanced by the fact that this cell is situated closer to the bed than SVO1. The

457   predicted inward and upward movement of near-bed fluid at this location is consistent with the pattern

458   of thermal mixing, which indicates that cooler water from the Kaskaskia River is convected into the

459   slightly warmer flow from the Copper Slough near the bed and that this convected fluid moves

460   upward toward the surface on the east side of the downstream channel [*Rhoads and Sukhodolov*,

461   2001].

462   Part of the reason for the rapid decay of the core of high u_s on the west side of the section is

463   related to the vortical structures within shear layers that form as fluid flows over the submerged bar of

464   failed bank material upstream (near section A3). At section C, these energetic eddies occupy most of

465   the west side of the channel section (see Fig. 2) and their vorticity is comparable to that of the mixing-

466   interface eddies. The eddies induced by the submerged bar enhance momentum exchange, flow

467   uniformity, and turbulence intensity. Peak values of u_s in section C occur in the vicinity of the bed

468   rather than close to the free surface. Also, the position of the region for which u_s>0.55 m/s is skewed

469   toward the inner (east) side of the section. The DES predicts that the largest streamwise velocities are

470   situated in the central part of the section close to the bed - a feature of the measured u_s distribution in

471   section C that is not captured well by the RANS model. The shapes of the isovels corresponding to

472   u_s=0.5-0.55 m/s in the RANS simulation differ substantially from the measured ones. The primary

473   reason for disagreements of the RANS results with the field measurements is underprediction of the

474   strength of the SOVs on both sides of the section.

475   The TKE distributions at sections A3, A1, A and C (Fig. 10) provide relevant information on

476   the complex structure of the turbulence within the junction region. DES correctly predicts the TKE

477   amplification adjacent to the separation zone near the upstream junction corner (section A3) where a

478   shear layer develops between this zone and incoming flow from the Copper Slough. Peak values of

479   TKE at this section in DES and the field experiment are close to 100 cm^2/s^2. In agreement with the

480   field observations, the mixing interface is nearly vertical and the largest TKE values occur in the

481   lowest portion of the layer.

482   Sections A1 and A intersect two regions where strongly energetic eddies are convected

483   downstream. The first one is the mixing interface situated in the central part of the section. The

484   second region, located near the west bank, is induced by the flow over the submerged bar situated

485   immediately downstream of section A3. The two regions are separated at sections A1 and A by the

486   core of high velocity originating in the central part of the KR tributary. The passage of strongly

487   energetic eddies induces substantial amplification of the turbulence intensity within these two regions.

488   DES results show that the size of the region of high TKE amplification near the west bank and the

489   peak TKE value within this region nearly double between sections A1 and A.

490   The peak values predicted by DES in the central part of sections A1 and A are close to 70

491   cm^2/s^2 and 60 cm^2/s^2, respectively. The corresponding measured values are 80 cm^2/s^2 and 70 cm^2/s^2,

492   respectively. In reasonable agreement with the field experiment, the region of high turbulence

493   amplification lies between the two cores of high streamwise velocity close to the free surface. The

494   location of the peak values of TKE differ slightly between the field measurements and the DES.

495   Whereas the field measurements indicate that the highest values of TKE occur close to the center of

496   the mixing interface, the DES predicts the highest values of TKE toward the center of the SOV cell on

497   the Copper Slough side of the mixing interface.

498   In the DES, the strong TKE amplification is due to unsteadiness of SOV cell position.

499   Animations show that the cores of the primary SOV cells, and in particular that of SVI1, are subject to

500   large-scale oscillations in the transverse (cross-stream) direction. Consistent with the stronger

501   circulation of the SOV cells (SVI1 and SVI2) on the CS side of the confluence, TKE amplification is

502   larger on the CS (east) side compared to the KR (west) side. Though the TKE peaks close to the

503   streamwise axis of SVI1 at both sections, the peak is shifted slightly toward the channel bottom. The

504   oscillating SVI1 cell interacts with the bed to produce tongues of vorticity of opposite sign that are

505   ejected from the bottom attached boundary layer beneath this cell. Thus, the development and

506   unsteadiness of the SOV cells strongly affects the turbulence structure in the central part of these two

507   sections.

508   As the cores of the SOVs oscillate along the margins of the mixing interface, they deflect

509   laterally the mixing interface and embedded eddies. Although details of the locations of the zone of

510   peak TKE differ slightly between the field measurements and DES, large-scale transverse oscillations

511   of the SOV cells probably explain why root-mean-square (rms) values of the transverse velocity

512   fluctuations in the field data [*Sukhodolov and Rhoads*, 2001] are comparable to the rms values of the

513   streamwise velocity within the region of high TKE. By contrast, the rms of the streamwise velocity is

514   around two times larger than the rms of the transverse velocity in straight river reaches in which the

515   flow is fully developed [*Sukhodolov et al*., 1998].   Large-scale oscillations of the mixing interface at

516   this confluence were documented by Rhoads and Sukhodolov (2004), who attributed low-frequency

517   peaks in spectral density functions of fluctuating components of streamwise and transverse velocities

518   to such oscillations.

519   The distribution of TKE at section C changes dramatically compared to distributions at

520   sections A1 and A. Here the region of turbulence amplification extends over most of the section. TKE

521   values predicted by DES within this region are between 20 and 50 cm^2/s^2, which is in good agreement

522   with the field measurements (20-40 cm^2/s^2). The mixing interface is not distinct from regions of high

523   TKE induced by the submerged bar of failed bank material on the west side of the section and, to a

524   lesser extent, by the shear layer forming in the region of high bank curvature on the CS side of the

525   section (Fig. 2). Still, two patches of high TKE can still be identified on the two sides of the mixing

526 layer in the DES results. They correspond to the cores of the two primary SOV cells. Consistent with

527 the fact that $\Gamma_{SVII} > \Gamma_{SVOI}$ (Fig. 6), the TKE amplification is greatest where the core of SVI1 is subject

528 to large-scale oscillations. The DES is not able to capture fully the high TKE near the bed in the field

529 measurements.

530   The RANS results for TKE do not compare favorably with the field data and DES. The best

531 agreement occurs near the upstream junction corner (section A3), where the RANS model predicts the

532 formation of regions of high TKE on each side of stagnation zone. The two regions of high TKE

533 correspond to the two separated shear layers bordering this zone of recirculating fluid. The TKE

534 values within the shear layers are smaller but comparable to those predicted by the field experiment

535 and DES around the centerline of the mixing interface.

536   The agreement worsens dramatically downstream at sections intersecting the mixing

537 interface. Because the RANS model severely underpredicts the coherence and circulation of the SOV

538 cells, it does not capture the TKE amplification within the cores of the primary SOVs in sections A1,

539 A and C. The RANS simulation even fails to predict the amplification of the TKE within the mixing

540 interface region, mainly because the mean shear between the two streams is small. Although RANS

541 models generally predict reasonably well flows in which the turbulence production is driven by mean

542 shear, the KH mode is weak for the flow examined here. Predicting TKE amplification of a mixing

543 interface in the wake mode is much more difficult for a steady RANS model because turbulence

544 production is related to vortex shedding rather than mean shear. RANS models are known to have

545 difficulties in predicting the turbulence structure in flows dominated by large-scale vortex shedding

546 (e.g., wake region of flow past bluff bodies). Thus, the RANS simulation fails to predict any of the

547 major features of the TKE distribution downstream of the confluence apex. This failure is linked to

548 limitations of the RANS model to predict the turbulence production and dissipation in regions

549 dominated by the presence of large-scale energetic eddies.

550

551 *6.3. Coherent structures and patterns of bed friction velocity: DES*

552	An important feature of the predicted spatial distribution of the dimensionless bed friction

553	velocity u_τ/U is that within the confluence and downstream channel (sections A1, A, C) the largest

554	values of u_τ/U occur beneath the primary SOV cells and the secondary SOV cell (SVI2) situated on

555	the east side of the confluence (Fig. 12). This finding implies that the SOV cells generate large values

556	of bed shear stress in the region of maximum confluence scour. Although the bed was not mobile

557	during the flow examined here, the findings imply that the SOV cells may play an important role in

558	maintaining scour at this confluence. Rhoads (1996) found that helical motion is strong during

559	transport effective flows at KRCS and sweeps sediment laterally away from the center of the

560	confluence toward the banks. A related result of the DES is that average levels of u_τ/U in the central

561	part of the downstream channel are lower beneath the mixing interface than beneath the primary SOV

562	cells. The wake mode of vortex formation generates eddies that increase in size, but vary little in

563	circulation as they are convected downstream. Thus, the capacity of these eddies to induce large bed

564	friction velocities is low at large distances from the upstream junction corner. In contrast to a mixing

565	interface in which the KH mode is strong, no mechanism exists in wake mode for vortex pairing and

566	increasing vortex circulation. As the angle between the two tributaries decreases and/or the difference

567	between the momentum fluxes of the two tributaries increases – factors that favor the KH mode,

568	levels of u_τ/U in the mixing interface region should increase with respect to levels beneath the SOV

569	cells.

570	The presence of a core of large streamwise velocity in the near bed region around the position

571	of section C (Fig. 9b) explains the persistence of large values of u_τ/U in the central part of the

572	downstream channel at streamwise locations where a significant decay in the coherence of the primary

573	SOV cells is observed. The persistence of this submerged core of high velocity at high transport-

574	effective flows probably contributes to maintenance of the scour hole at KRCS [*Rhoads*, 1996]. Local

575	effects, such as strong acceleration of flow over the failed blocks of bank material near the west bank

576	around section A3 can also produce patches of high bed friction velocity.

577	At any given time instant, the SOV cells are characterized by a large non-uniform variation of

578	their coherence in the streamwise direction (Figure 13). Despite this variation, the position of patches

579   of high streamwise vorticity between sections A2 and B correlates closely to the position of the SOV

580   cells as given by the Q criterion. In the instantaneous flow fields, the core of SVI1 loses most of its

581   coherence by section C. Downstream of section B, the predominantly streamwise-oriented eddies

582   detaching from the downstream part of SVI1 are strongly stretched by the surrounding turbulence,

583   thereby increasing their three-dimensionality and creating conditions for their breakup into smaller 3D

584   eddies. A similar scenario occurs on the other side of the mixing interface where it is hard to

585   distinguish between the streamwise-oriented eddies associated with SVO1 and the surrounding large-

586   scale 3D eddies generated by the flow past the submerged bar of failed bank material along the west

587   bank. The 3D eddies strongly jitter the patches containing predominantly streamwise vorticity

588   detaching from the downstream part of SVO1. This effect contributes to the diminution of SVO1

589   compared to SVI1.

590   The large-scale eddy content of the region situated between SVI1 and SVO1 is low. In

591   particular, at most times few vertically oriented eddies are observed in this region. For example, only

592   one such eddy - located at a short distance downstream of section A on the east side of the mixing

593   interface - can be clearly identified in Fig. 13. This result supports the claim that for the geometrical

594   and flow conditions considered in the present test case, the coherence of the quasi-2D mixing layer

595   eddies is substantially less than that of the SOV cells not only in the instantaneous flow but, even

596   more important for patterns of erosion and deposition, also in the mean flow fields.

597   The distribution of u_τ/U in the mean flow provides only partial information on patterns of bed

598   shear stresses that may result in erosion and deposition. If an eddy is sufficiently large such that the

599   time over which values of the bed friction velocity remain larger than the critical value for sediment

600   entrainment is sufficiently long, then substantial mobilization of sediment will occur at that location

601   during the passage of the eddy.   The association between a strongly coherent vortical eddy associated

602   with the core of one of the SOV cells and high values of bed friction velocity is high upstream of

603   section B (Fig. 14). Between the confluence apex and section B, the cores of the SOV cells are

604   twisting in time around axes that vary in distance from the bed over relatively small streamwise

605   distances. Thus, even where the coherence of the SOV cells is high, the zone of amplification of the

606   bed friction velocity will vary depending on the distance of the axis of vorticity from the streambed.

607   Occasionally, a strongly coherent mixing-interface eddy can also induce large values of the

608   bed friction velocity (see Fig. 14). The level of amplification of the bed friction velocity beneath such

609   an eddy is sometimes similar to that observed beneath the regions of high coherence of the SOV cells.

610   However, at any given time, the area of the bed surface region in which the bed friction velocity is

611   amplified by the passage of the mixing-interface eddies is much smaller than the region in which the

612   bed friction velocity is amplified by near-bed SOVs. Thus, the SOV cells appear to have the dominant

613   influence on the pattern of bed friction velocity for the flow investigated here.

614

615   **7. Summary and concluding remarks**

616   An eddy-resolving simulation (DES) was used to explore the three-dimensional structure of

617   time-averaged and instantaneous flow at an asymmetrical river confluence with a concordant bed for

618   which the momentum ratio is close to one. The results of the simulation were compared to field data

619   on mean flow and turbulence for the flow event. The DES provides a more detailed depiction of the

620   flow and turbulent structure in the confluence hydrodynamic zone than can be derived from field data

621   [*Rhoads and Sukhodolov,* 2001]. In particular, it facilitates visualization of dynamically important

622   coherent structures over the entire flow domain as well as estimation of quantities that are difficult to

623   measure in the field or even in the laboratory (e.g., bed friction velocity).

624   The DES successfully captured the development of streamwise-oriented-vortical (SOV) cells

625   on both side of the confluence and allowed a quantitative characterization of their position and

626   strength (e.g., as characterized by the streamwise variation of the circulation). Equally important,

627   DES showed how large-scale coherent structures, such as SOV cells, mixing-interface eddies, and

628   locally-generated vortical features, influence patterns of mean streamwise velocity and turbulent

629   kinetic energy induced by the complex geometry of the confluence. For example, the DES highlights

630   how large amplification of the TKE in the central part of cross-sections situated downstream of the

631   upstream junction corner is mainly due to the cross-stream (transverse) oscillations of the SOV cells.

632   Such oscillations provide an explanation for why transverse velocity fluctuations in the field

633   experiment and DES are comparable to or larger than streamwise velocity fluctuations.

634 Finally, the simulation of instantaneous turbulent flow provided the basis for assessing how

635 mixing-interface eddies, SOV cells and the other large scale turbulent structures influence the pattern

636 of bed friction velocity and the contributions of various coherent aspects of the flow to maintenance

637 of bed morphology, including confluence scour. This capability is critical for understanding how the

638 passage of large-scale energetic eddies (e.g., quasi 2D mixing layer vortices) over the bed can induce

639 instantaneous or short-duration bed shear stresses that greatly exceed mean bed shear stresses, thereby

640 mobilizing sediment and contributing to maintenance or restructuring of bed morphology.

641 The study showed that the use of eddy resolving techniques to compute the flow resulted in

642 more accurate predictions of the distributions of the mean streamwise velocity and turbulent kinetic

643 energy compared to results from a steady RANS model. The main reason for the poor level of

644 agreement of the RANS simulation with the measured data is substantial underprediction of the

645 coherence and circulation of the SOV cells.

646 Visualization of eddies in the instantaneous flow fields confirmed that the mixing interface is

647 populated by quasi 2D eddies. However, the structure of the mixing interface differed from the

648 classical case of a mixing layer developing between two parallel streams with a high momentum ratio,

649 where eddies are co-rotating and the growth of the mixing layer is driven by vortex pairing (Kelvin-

650 Helmholtz mode). In the case analyzed at the KRCS confluence, successively shed eddies rotate in

651 opposite directions. Thus, the mixing-interface structure resembles that of the wake behind a bluff

652 body (wake mode). The strength of the wake mode depends on the details of flow stagnation and the

653 dynamics of the shear-layer bounding the region of stagnation near the upstream junction corner.

654 Farther downstream, the coherence of eddies in a mixing interface in which the wake mode is

655 dominant is significantly less than that of eddies in which the KH mode is strong. Their weak

656 coherence limits the contribution of quasi-2D eddies to the bed friction velocity for a mixing interface

657 in the wake mode. Factors that favor the wake mode include a high junction angle, which promotes

658 flow stagnation, and $M_r \approx 1$, which minimizes lateral shear between the confluent flows. Rhoads and

659 Sukhodolov (2008) argued that wakes effects also are important at KRCS when $M_r \gg 1$; further DES

660 modeling is needed to evaluate the extent to which the wake mode influences flow structure in the

661 mixing interface at high momentum ratios.

662   The present study demonstrates that SOV cells of helical motion associated with the

663   formation of strong vortical eddies beneath the free surface on both sides of the mixing interface are a

664   prominent feature of the flow structure at a confluence with a large angle between the two tributaries

665   and with a momentum ratio close to unity (mixing interface in the wake mode). A main finding of the

666   study is that for this type of confluence, the primary and secondary SOV cells are the main coherent

667   flow structures responsible for the amplification of the bed friction velocity. The occurrence of dual,

668   counter-rotating SOV cells at KRCS has been documented in previous field studies [*Rhoads*, 1996;

669   *Rhoads and Kenworthy*, 1998; *Rhoads and Sukhodolov*, 2001], but the level of resolution of the field

670   measurements was not sufficient to evaluate whether multiple helical cells exist on each side of the

671   mixing interface as predicted by the DES. More detailed field studies are needed to evaluate the DES

672   predictions of multiple SOV cells at asymmetrical confluences.

673   The study has also shown that for natural confluences, the streamwise development of the

674   SOV cells and of the mixing interface can be strongly affected by the presence of large-scale

675   irregularities at the banks or on the channel bed (e.g., the presence of a submerged block of failed

676   bank material at the west bank) or by strong curvature of the channel banks. Interaction between local

677   vortices in shear layers generated by irregulaties and the mixing interface leads to complex patterns of

678   turbulence. These local vortices also interact with SOVs and may modify the strength of these cells.

679   Thus, confluences with strong local effects may not have well-developed SOV cells ([*Rhoads and*

680   *Sukhodolov*, 2001].

681

689

690   **References**

691   Ashmore, P.E., Ferguson, R.I, Prestegaard, K.L., Ashworth, P.J., and Paola, C. (1992), Secondary

692   flow in anabranch confluences of a braided, gravel-bed stream, *Earth Surf. Processes*

693   *Landforms*, 17, 299-311.

694   Ashmore, P., and G. Parker (1983), Confluence scour in coarse braided streams, *Water Resources*

695   *Research*, *19*, 392-402.

696   Babarutsi, S., and V. H. Chu (1998), Modelling transverse mixing layer in shallow open-channel

697   flows, *Journal of Hydraulic Engineering*, *124*, 718-727.

698   Best, J. L. (1988), Sediment transport and bed morphology at river channel confluences,

699   *Sedimentology*, *35*, 481-498.

700   Best, J. L., and I. Reid (1984), Separation zone at open-channel junctions, *Journal of Hydraulic*

701   *Engineering*, *110*, 1588-1594.

702   Best, J. L., and B. L. Rhoads (2008), Sediment transport, bed morphology and the sedimentology of

703   river channel confluences, in *River Confluences, Tributaries and the Fluvial Network* edited by

704   S. P. Rice, et al., pp. 45-72, John Wiley and Sons Chichester.

705   Biron, P., De Serres, B. and Best, J.L. (1993a), Shear layer turbulence at unequal depth channel

706   confluence, in *Turbulence: Perspectives on Flow and Sediment Transport*, edited by N. J.

707   Clifford, et al., pp. 197-213, John Wiley & Sons Ltd, New York.

708   Biron, P., Roy, A.G., Best, J.L. and Boyer, C.J. (1993b), Bed morphology and sedimentology at the

709   confluence of unequal depth channels, *Geomorphology*, 8, 115-129.

710   Biron, P. M., Richer, A., Kirkbride, A.D., Roy, A.G. and Han, S. (2002), Spatial patterns of water

711   surface topography at a river confluence, *Earth Surf. Process. Landf.*, *27*, 913-928.

712   Bouchez, J., Lajeunesse, E., Gaillardet, J., France Lanord, C., Dutra Maia, P. and Maurice, L.

713   (2010), Turbulent mixing in the Amazon River: The isotopic memory of confluences, *Earth*

714   *Planet. Sci. Lett.*, *290*, 37-43.

715   Boyer, C., Roy, A. G., Best, J. L. (2006), Dynamics of a river channel confluence with discordant

716   beds: Flow turbulence, bed load sediment transport, and bed morphology, *J. Geophysical*

717   *Research-Earth Surface*, 111, F04007.

718   Bradbrook, Lane, S.N. and Richards, K.S. (2000a), Numerical simulation of three dimensional time-

719   averaged flow at river channel confluences, *Water Resources Research*, 36, 2731-2746.

720   Bradbrook, K. F., Lane, S.N., Richards, K.S., Biron, P. and Roy, A.G. (2000b), Large Eddy

721   Simulation of periodic flow characteristics at river channel confluences, *Journal of Hydraulic*

722   *Research*, *38*, 207-215.

723   Bradbrook, K.F., Lane, S.N., Richards, K.S., Biron, P. and Roy, A.G. (2001), Role of bed

724   discordance at asymmetrical open-channel confluences, *Journal of Hydraulic Engineering*, 127,

725   351-368.

726   Chang, K.S., Constantinescu, G. and Park, S.O. (2007), Assessment of predictive capabilities of

727   Detached Eddy Simulation to simulate flow and mass transport past open cavities, *ASME*

728   *Journal of Fluids Engineering*, 129(11), 1372-1383.

729   Chu, V. H., and S. Babarutsi (1988), Confinement and bed-friction effects in shallow turbulent

730   mixing layers, *Journal of Hydraulic Engineering*, *114*, 1257-1274.

731   Constantinescu, G. and Squires, K.D. (2004), Numerical investigation of the flow over a sphere in

732   the subcritical and supercritical regimes, *Physics of Fluids*, 16(5), 1449-1467.

733   Dubief, Y. and Delcayre, F. (2000), On coherent vortex identification in turbulence, *Journal of*

734   *Turbulence*, 1-011.

735   Ferguson, R.I., Parsons, D.R., Lane, S.N. and Hardy, R.J. (2003), Flow in meander bends with

736   recirculation at the inner bank, Water Resources Research, 39(11), 1322.

737   Kenworthy, S.T. and Rhoads, B.L. (1995), Hydrologic control of spatial pattern of suspended

738   sediment concentration at a small stream confluence. *Journal of Hydrology*, 168, 251-263.

739   Kirkil, G. and Constantinescu, S.G. (2008), A numerical study of shallow mixing layers between

740   parallel streams, *2ⁿᵈ International Symposium on Shallow Flows*, Hong Kong, December 2008.

741   Kirkil, G. and Constantinescu, G. (2009), Nature of flow and turbulence structure around an in-
742   stream vertical plate in a shallow channel and the implications for sediment erosion, *Water*
743   *Resources Research*, 45, W06412, doi:10.1029/2008WR007363.

744   Kirkil, G., Constantinescu, G. and Ettema, R. (2009), DES investigation of turbulence and sediment
745   transport at a circular pier with scour hole, *Journal of Hydraulic Engineering,* 135(11), 888-901.

746   Koken, M. and Constantinescu, G. (2009), An investigation of the dynamics of coherent structures in
747   a turbulent channel flow with a vertical sidewall obstruction, *Physics of Fluids*, 21, 085104, DOI
748   10.1063/1.3207859.

749   MacKay, J. R. (1970), Lateral mixing of the Liard and Mackenzie rivers downstream from their
750   confluence, *Canadian Journal of Earth Sciences*, *7*, 111-124.

751   McCoy, A., Constantinescu, G. and Weber, L. (2007), A numerical investigation of coherent
752   structures and mass exchange processes in a channel flow with two lateral submerged groynes,
753   *Water Resources Research,* 43, W05445, DOI:10.1029/2006WRR005267.

754   Paola, C. (1997) When streams collide. *Nature*, 387, 232-233.

755   Rhoads, B. L. (1996), Mean structure of transport-effective flows at an asymmetrical confluence
756   when the main stream is dominant. In *Coherent Flow Structures in Open Channels,* edited by
757   Ashworth, P.J., Best, J.L., Bennett, S.L. and McLelland, S.J., 491-517, J. Willey, New York.

758   Rhoads, B.L., and Kenworthy, S.T. (1995), Flow structure at an asymmetrical stream confluence.
759   *Geomorphology,* 11, 273-293.

760   Rhoads, B.L., and Kenworthy, S.T. (1998), Time-averaged flow structure in the central region of a
761   stream confluence, *Earth Surf. Proc. Land.,* 23, 171-191.

762   Rhoads, B. L., and S. T. Kenworthy (1999), On secondary circulation, helical motion and Rozovskii-
763   based analysis of time-averaged two-dimensional velocity fields at confluences, *Earth Surf.*
764   *Process. Landf.*, *24*, 369-375.

765   Rhoads, B.L., Riley, J.D., and Mayer, D.R. (2009) Response of bed morphology and bed material
766   texture to hydrological conditions at an asymmetrical stream confluence, *Geomorphology, 109,*
767   *161-173.*

768   Rhoads, B. L. and Sukhodolov, A. N. (2001), Field investigation of three-dimensional flow structure

769   at stream confluences: 1. Thermal mixing and time-averaged velocities, *Water Resources*

770   *Research*, 37 (9), 2411-2424.

771   Rhoads, B.L. and Sukhodolov, A.N. (2004), Spatial and temporal structure of shear layer turbulence

772   at a river confluence, *Water Resources Research*, 40, W06304.

773   Rhoads, B. L., Sukhodolov, A. N. (2008), Lateral momentum flux and spatial evolution of flow

774   within a confluence mixing interface, *Water Resources Research*, 44, WR08440;

775   doi:10.1029/2007WR006634.

776   Spalart, P. (2000), Trends in turbulence treatments, AIAA Paper 2000-2306, *38th AIAA Aerospace*

777   *Sciences Meeting and Exhibit*, Reno, Nevada, USA.

778   Spalart, P. (2009), Detached eddy simulation, *Annual Review of Fluid Mechanics*, 41, 181-202.

779   Sukhdolov, A. N. and Rhoads, B. L. (2001), Field investigation of three-dimensional flow structure

780   at stream confluences. *Water Resources Research*, 37, 2393-2410.

781   Weerakoon, S.B. and Tamai, N. (1989), Three dimensional calculation of flow structure in channel

782   confluences using boundary-fitted coordinates, *J. Hydrosci. Hydraul. Eng.*, 7, 51-62.

783   Winant, C. D., and F. K. Browand (1974), Vortex pairing: the mechanism of turbulent mixing layer

784   growth at moderate Reynolds numbers, *Journal of Fluid Mechanics*, *63*, 237-255.

785   Zeng, J., Constantinescu, S. G., Blanckaert., K., and Weber, L. (2008), Flow and bathymetry in

786   sharp open-channel bends: Experiments and predictions, *Water Resources Research*, 44 (9),

787   W09401.

788
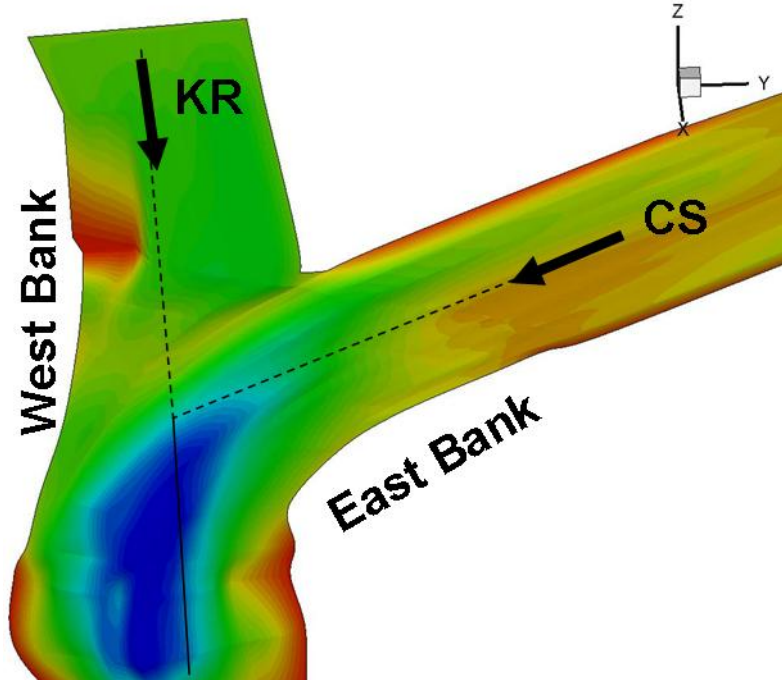
Figure 1. Computational domain around the confluence between the Kaskaskia River (KR) and Copper Slough. The bathymetry is visualized using bed elevation contours.
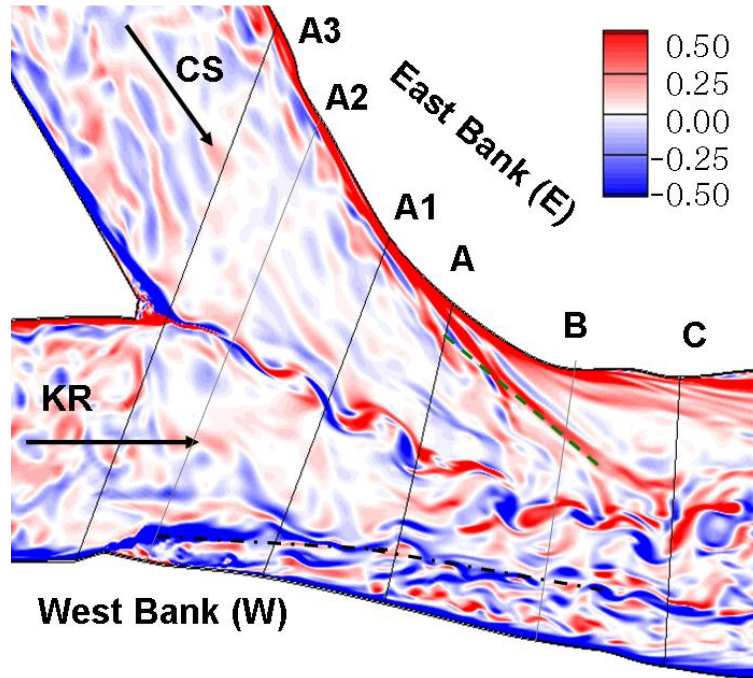
Figure 2 Distribution of the vertical vorticity, $\omega_z D/U$, in the instantaneous flow in a horizontal surface situated at 0.1D below the free surface. Also shown are the positions of the cross-sections where the mean flow and turbulence structure will be analyzed. The dashed line visualizes the shear layer forming at the East bank due to the strong curvature of the inner bank. The dashed-dotted line visualizes the separated shear layer forming due to the presence of a submerged bar of failed bank material at the West Bank, near section A3 (see also Fig. 1).
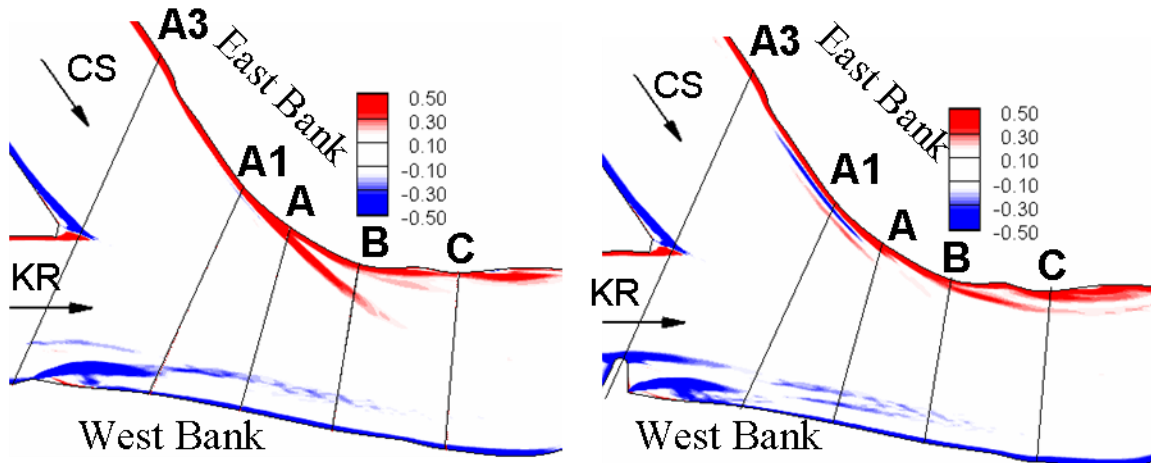
799
800 Figure 3 Distribution of the vertical vorticity, $\omega_z D/U$, in the mean flow at the free surface (left) and at
801 0.5D below the free surface (right).
802
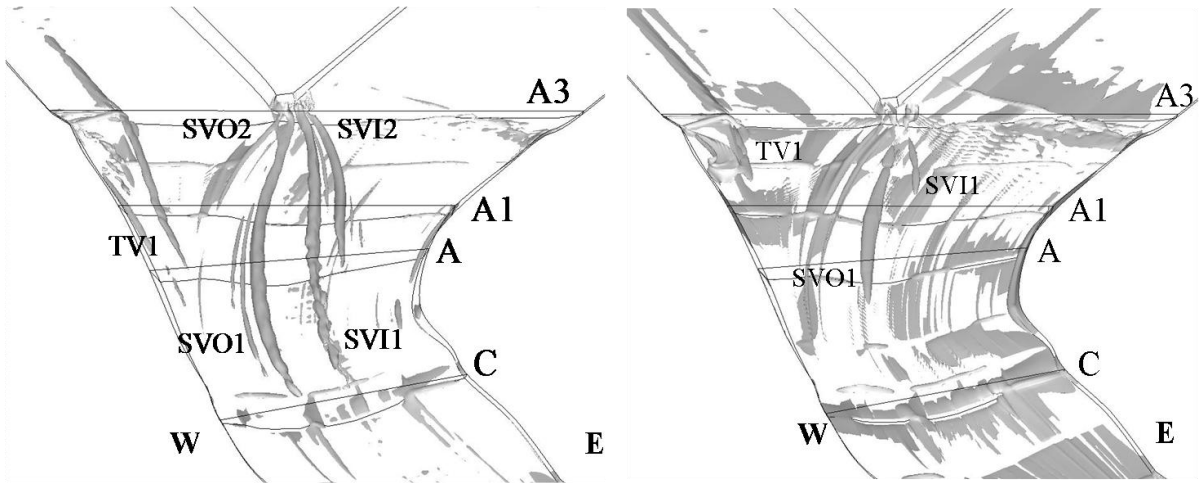
803
804 Figure 4. Visualization of the main vortical structures in the mean flow predicted by the DES (left)
805 and RANS (right) simulations using the Q criterion.
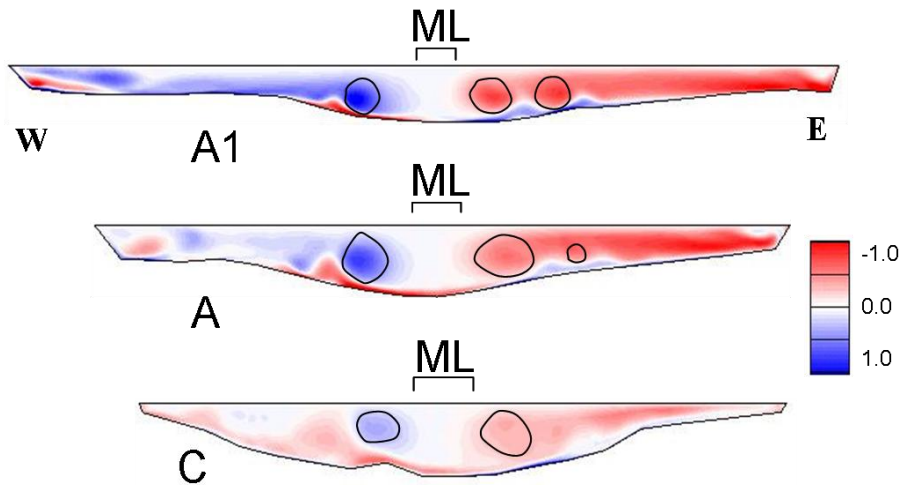
806
807
808 Figure 5. Distribution of the streamwise-oriented vorticity, $\omega_s D/U$, in the mean flow at sections A1, A
809 and C (DES simulation). The solid lines show the cores of the streamwise-oriented vortices in the
810 three sections, as visualized by the Q criterion (see also Fig. 3a). ML denotes the local width of the
811 mixing layer in each section.
812
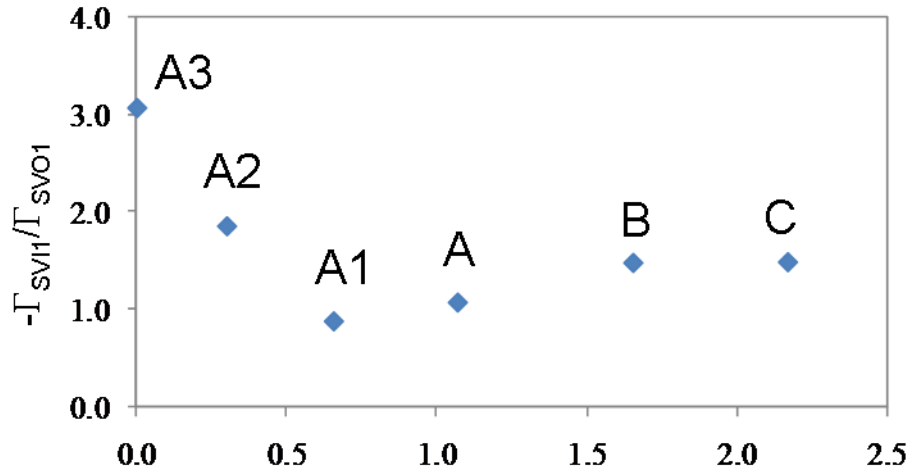
813
814 Figure 6. Variation of the ratio, $-\Gamma_{SVI1}/\Gamma_{SVO1}$, between the circulation of the main streamwise-oriented
815 vortices SVI1 and SVO1 on the two sides of the mixing layer with the non-dimensional distance from
816 upstream junction corner, s/W (W=14D is the average width of the downstream channel).

817
818
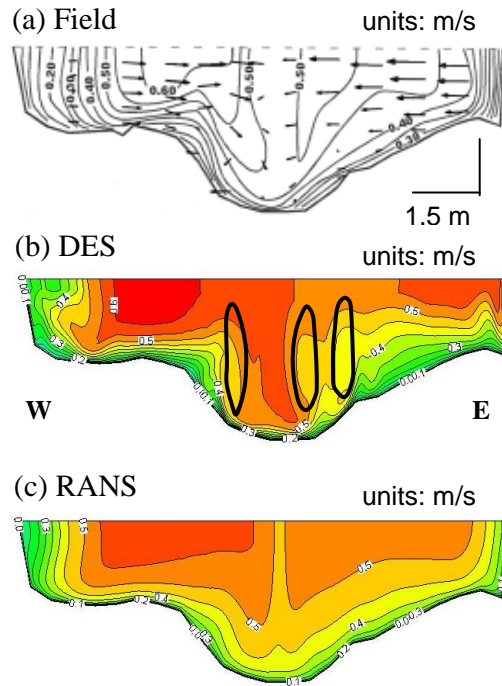
819
820 Figure 7. Distribution of the mean streamwise velocity, u_s (m/s), in section A1. a) field experiment; b)
821 DES; c) RANS. The scale is distorted in the vertical direction (aspect ratio is 1:0.208). The solid lines
822 visualize the position of the main streamwise-oriented vortices in the section.

(a) Field units: m/s

(b) DES units: m/s

W E

(c) RANS units: m/s
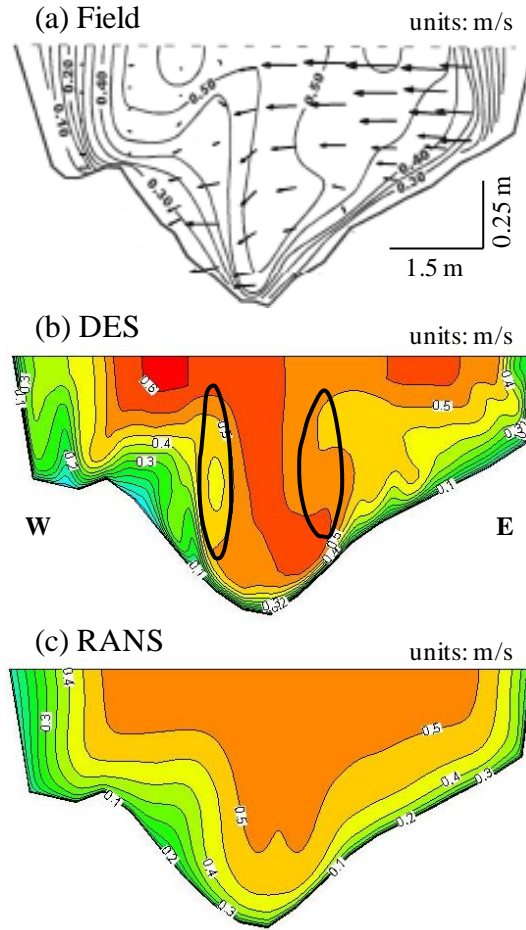
823
824 Figure 8. Distribution of the mean streamwise velocity, u_s (m/s), in section A. a) field experiment; b)
825 DES; c) RANS. The scale is distorted in the vertical direction (aspect ratio is 1:0.208). The solid lines
826 visualize the position of the main streamwise-oriented vortices in the section.
827
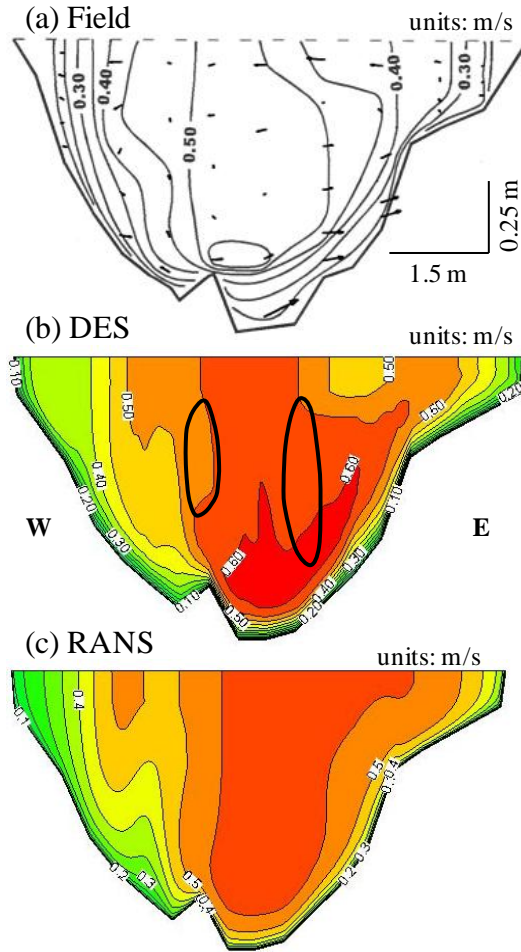
829 Figure 9. Distribution of the mean streamwise velocity, u_s (m/s), in section C. a) field experiment; b)
830 DES; c) RANS. The scale is distorted in the vertical direction (aspect ratio is 1:0.208). The solid lines
831 visualize the position of the main streamwise-oriented vortices in the section.
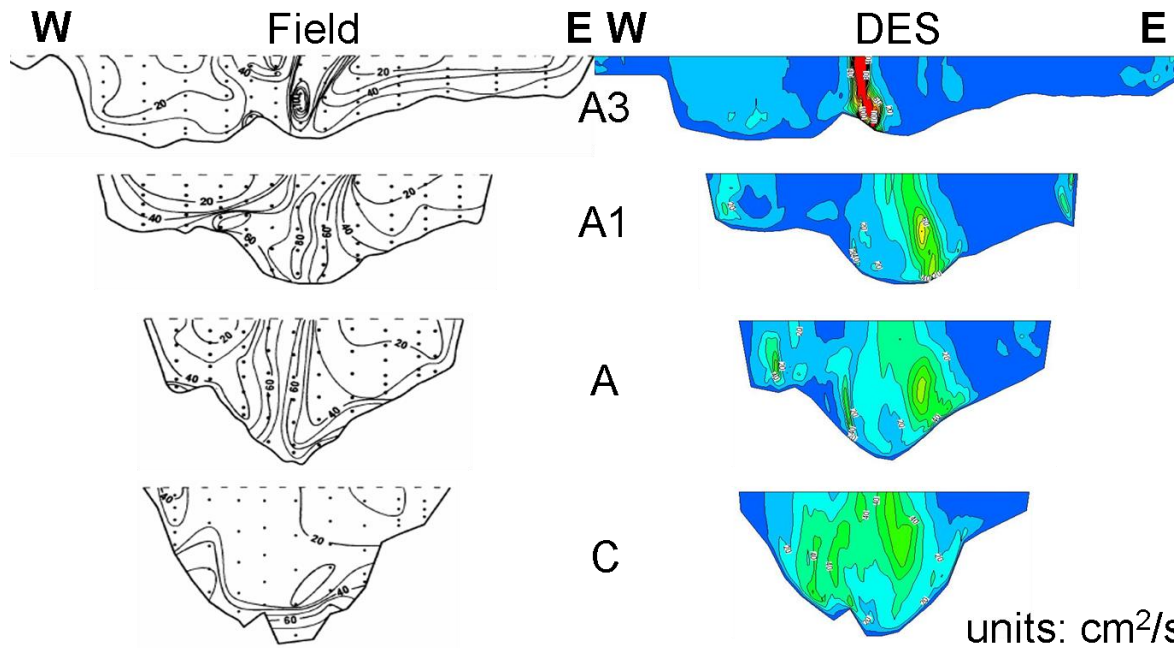
833 Figure 10. Distribution of the turbulent kinetic energy, TKE (cm^2/s^2) in sections A3, A1, A and C in
834 the field experiment (left) and DES simulation (right). The scale is distorted in the vertical direction
835 (aspect ratio is 1:0.208).
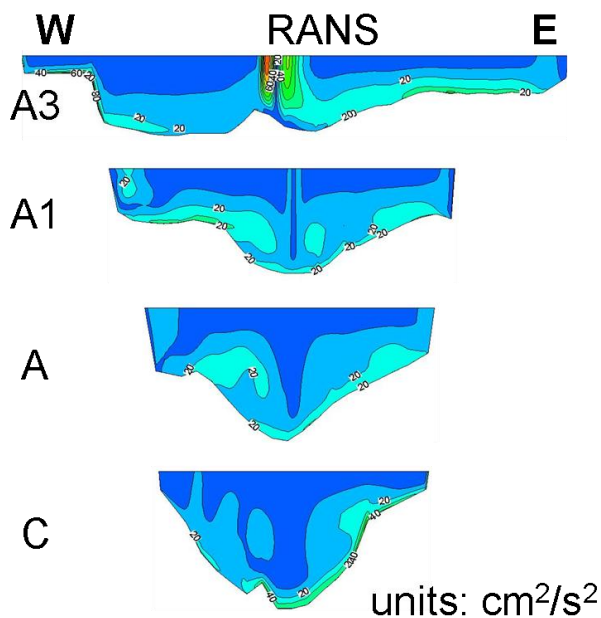
Figure 11. Distribution of the turbulent kinetic energy, TKE (cm^2/s^2) in sections A3, A1, A and C in the RANS simulation. The scale is distorted in the vertical direction (aspect ratio is 1:0.208).
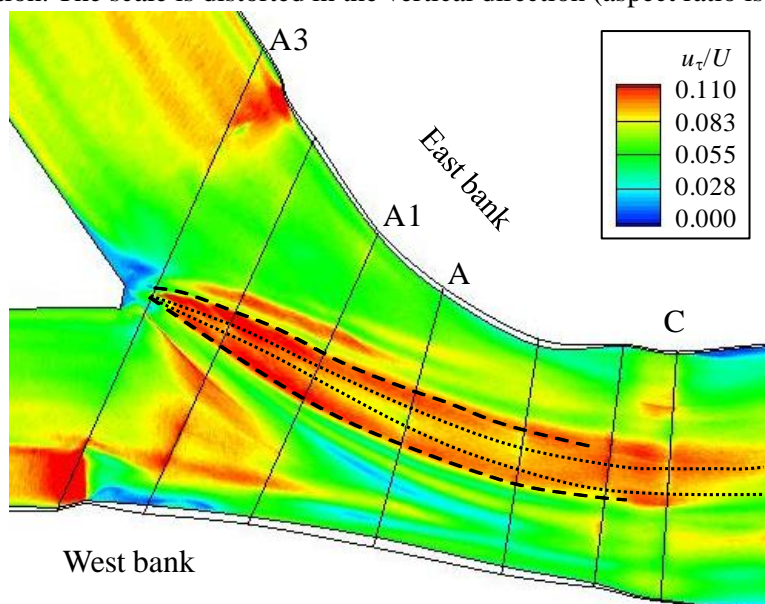
Figure 12. Distribution of the magnitude of the bed friction velocity, u_τ/U, in the mean flow. The dashed lines show the positions of the axes of the streamwise-oriented vortices SVI1 and SVO1. The dotted lines delimitate the lateral extent of the mixing layer.
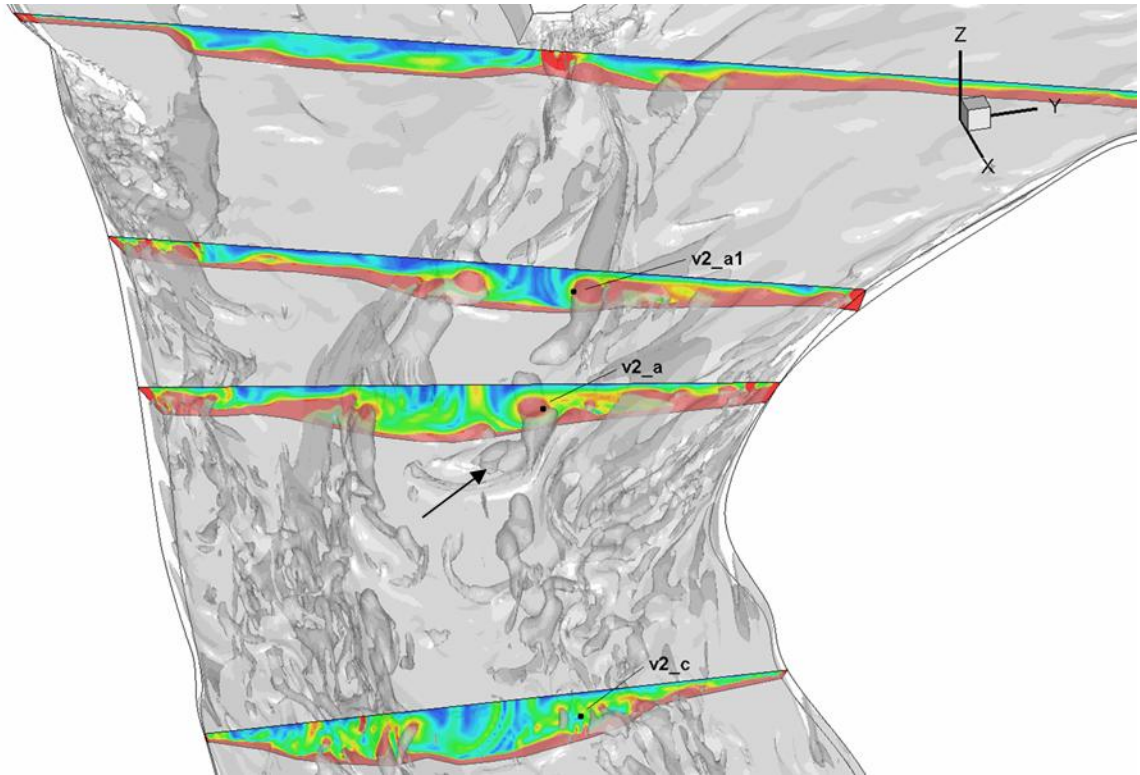
845
846 Figure 13. Visualization of the vortical structures predicted by the DES simulation in the
847 instantaneous flow using the Q criterion. Also shown are the distributions of the streamwise vorticity
848 at sections A3, A1, A and C. The solid lines point toward the core of SVI1 in sections A1, A and C.
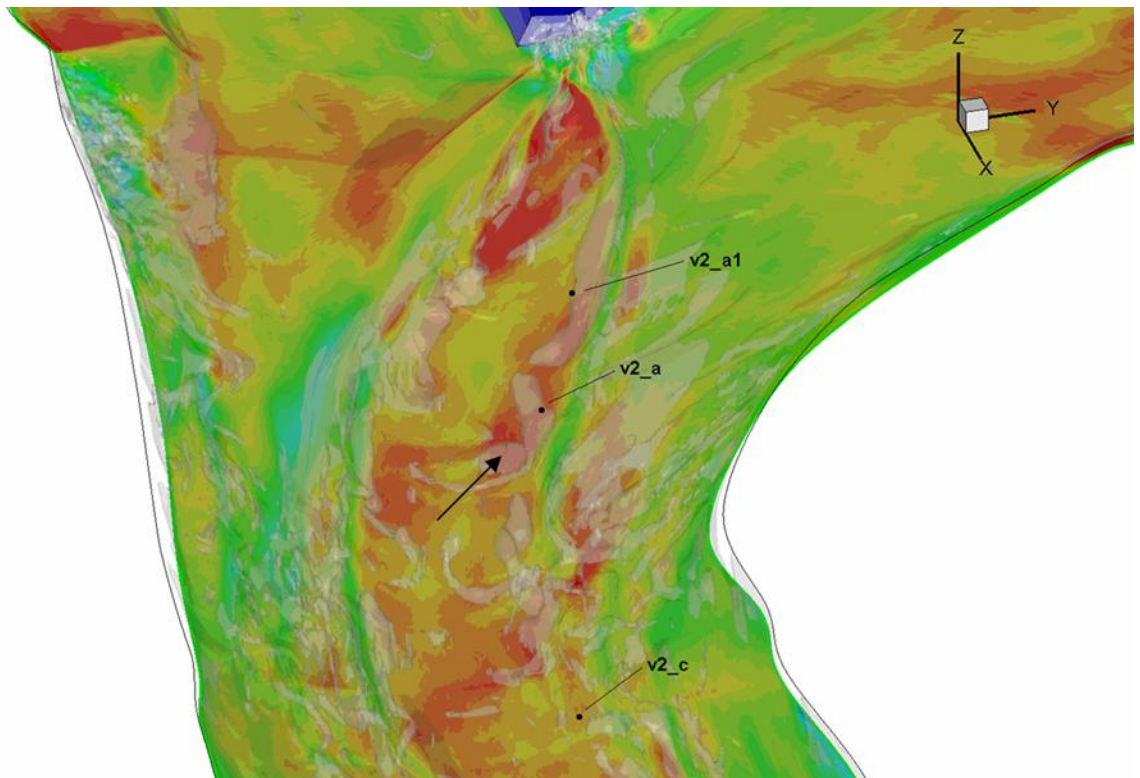849 The arrow points toward a vertically-oriented mixing layer eddy.
850

851
852 Figure 14. Distribution of the magnitude of the bed friction velocity, u_τ/U, in the instantaneous flow
853 (DES simulation). Also shown is the vortical structure of the flow at the same time instant, as
854 visualized by the Q criterion. The arrow points toward a vertically-oriented mixing layer eddy.
855